

Oxygen isotope ratios of HdC Stars

ABSTRACT

NOTE: Some parts are still a work in progress, and I am redoing fits for the stars after fixing an old mistake. This will have small effects on the A(C) and A(N) values reported in Table 4, but I don't expect much else to be changed (The Fig 4b correlation should stay). I have indicated a few other places where things need to be added or might be subject to change in red. I will be updating this draft regularly.

Update (November 25): I have finished re-analyzing and updated the tables and figures. I have to add X v/s Fe plots and update the discussion next.

R Coronae Borealis (RCB) and dustless Hydrogen-deficient Carbon (dLHdC) stars are supergiants with anomalous chemical abundances that suggest they are the remnants of He-CO white dwarf mergers. In addition to being hydrogen-deficient and carbon-rich, these stars have a stark overabundance of ^{18}O in their atmospheres. RCB stars are known to undergo carbon dust formation episodes that lead to drastic brightness variations, while dLHdC stars do not show such variability. While these stars have very similar chemical compositions, it is suggested that dLHdC stars have lower $^{16}\text{O}/^{18}\text{O}$ ratios than RCB stars. We aim to compare the oxygen isotope ratios of a sample of HdC stars to examine this claim.

We present high-resolution ($R \approx 75000$) K -band spectra of six RCB and six dLHdC stars, including four newly discovered dLHdC stars. We develop a semi-automated fitting routine to robustly estimate abundances and $^{16}\text{O}/^{18}\text{O}$ ratios for this sample, tripling the number of dLHdC stars with known oxygen isotope ratios and making this the largest sample of HdC stars with high-resolution NIR spectra to date. We find that all six dLHdC stars have $^{16}\text{O}/^{18}\text{O} < 1$, while the RCB stars show $^{16}\text{O}/^{18}\text{O} > 4$. Further, we observe a trend with effective temperature for RCB stars, with a pair of cold RCB stars conclusive shown to exhibit $^{16}\text{O}/^{18}\text{O} \sim 100$ for the first time.

Our results indicate that dLHdC stars have oxygen isotope ratios that are an order of magnitude lower than those of RCB stars. We find that the wide range of $^{16}\text{O}/^{18}\text{O}$ ratios observed in RCB stars and a trend with the effective temperature can be explained by existing binary white dwarf merger models. Current models, however, fail to predict or explain the low $^{16}\text{O}/^{18}\text{O}$ ratios observed in dLHdC stars, and an extension of model parameters is needed to explain these observations. Additionally, we discuss a possible detection of molecular CO emission lines from the circumstellar medium in RCB stars at maximum light for the first time.

1. INTRODUCTION

Hydrogen-deficient Carbon (HdC) stars are a class of supergiant stars with unusual chemical compositions, characterized by an acute deficiency of hydrogen and an overabundance of carbon (Clayton 1996, 2012; Lambert & Rao 1994). Their peculiar chemical compositions suggest that they originate in the merger of a He-core and a CO-core white dwarf (Clayton et al. 2005; Schwab 2019). Adding to their intrigue, HdC stars seem to comprise two varieties with similar chemical compositions but distinct photometric properties: R Coronae Borealis (RCB)-type stars that show erratic brightness variations resulting from dust ejection episodes, and dustless Hydrogen-deficient Carbon (dLHdC) stars that do not show dramatic brightness variations or any signs of dust

formation (Tisserand et al. 2020). Why RCB stars form dust while dLHdC stars do not despite having similar chemical compositions is still a mystery.

Several studies have attempted to identify chemical differences between RCBs and dLHdC stars as a step towards solving their dusty mystery. Using medium resolution K -band spectra of these stars covering the CO molecular absorption bandheads, Clayton et al. (2007) first noted that RCB stars and dLHdC stars possibly differ in their oxygen isotope ratios, with dLHdCs having $^{16}\text{O}/^{18}\text{O} < 1$, while RCBs having $^{16}\text{O}/^{18}\text{O} > 1$. This was confirmed with high-resolution spectra by García-Hernández et al. (2009, 2010). However, these studies were based on small samples of five RCB stars and two dLHdC stars. Although there were over fifty RCB stars

known at the time, only four dLHdC stars were known, of which two were too warm to exhibit CO lines. However, this has changed recently with the discovery of 27 new dLHdC stars (Tisserand et al. 2022). Additionally, a large number of RCB stars have been observed at near-infrared wavelengths have been more near-infrared spectroscopic observations (Karambelkar et al. 2021, 2024), enabling spectroscopic comparisons of larger samples of RCB and dLHdC stars.

Using medium resolution NIR spectra for the expanded sample of RCBs and dLHdCs, (Karambelkar et al. 2022) showed that dLHdC stars generally tend to have lower values of $^{16}\text{O}/^{18}\text{O}$ than RCBs, and suggested that this difference could be attributed to different masses or mass-ratios of the merging white-dwarfs Crawford et al. (2024). However, the oxygen isotope ratios measured from the medium resolution spectra have large uncertainties due to excessive blending with molecular CN lines in this wavelength range. This lack of precision precludes further insights, such as ..

In this paper, we present high resolution ($R \approx 75000$) K-band spectra of six RCB and six dLHdC stars. These spectra are the highest resolution NIR spectra of the largest sample of RCB and dLHdC stars to date. We use these spectra to derive the oxygen isotope ratios and other elemental abundances of these stars and examine differences between RCB and dLHdC stars. The paper is structured as follows - Section 2 describes the spectroscopic observations, Section 3.3 describes the abundance measurement method, 4 examines the differences and trends of the abundance measurements. We conclude with a summary of our results in Section 5.

2. OBSERVATIONS

Our data consists of high-resolution ($R \approx 75000$ or 4 km/s) K-band spectra of nine RCB and six dLHdC stars acquired with the iSHELL spectrograph (Rayner et al. 2022) on the 3.2 m NASA Infrared Telescope Facility (IRTF) at Mauna Kea Observatory, Hawaii. The observations were obtained over six nights between 2022 September 14 and 2022 October 3, with the 0.375" slit, using the K order sorter in the K_3 mode which covers the wavelength range of 2.26 – 2.55 μm . This region was chosen to include multiple bandheads of $^{12}\text{C}^{16}\text{O}$ and $^{12}\text{C}^{18}\text{O}$, as well as several lines of $^{12}\text{C}^{14}\text{N}$. The full log of observations is listed in Table 1. The spectra were reduced using the `idl` software `spextool` (Cushing et al. 2004), and were calibrated and corrected for telluric absorption using the `xtellcor` package (Vacca et al. 2003). Table 1 also lists the median signal-to-noise ratios for the spectra measured at the continuum level in the 2.3 – 2.4 μm region, which ranges from 32 to 127.

For the RCB stars in our sample, we determined their photometric phases at the epochs of the IRTF observations using time-series photometric information aggregated from various surveys by the DREAMS monitoring portal¹. Of the nine RCB stars, IRAS 1813+ and WISE J1820+ were observed in a decline, where their V-band brightness were fainter by $\Delta V \approx 1$ and $\Delta V \approx 3$ mag than maximum luminosity respectively. Subsequently, the spectra for these two stars have not been analyzed as the photospheric lines are heavily diluted by newly ejected dust clouds. Additionally, although it was observed at maximum light, V CrA was found to have a heavily diluted and featureless spectrum, due to a combination of its high estimated effective temperature (~ 6500 K) and large K-band excess due to circumstellar dust. ASAS-RCB-18 and ASAS-RCB-21 were recovering from decline phases and were both roughly 0.8 mag fainter than maximum luminosity, but this does not appear to appreciably dilute the photospheric spectrum. The remaining four RCB stars were observed at maximum light, bringing the total number of RCB stars analyzed in this work to six.

3. ABUNDANCE ANALYSIS

3.1. Notable Spectral Features

Our spectra cover several molecular absorption features such as the CN Red System of $^{12}\text{C}^{14}\text{N}$, the first seven overtone bandheads of $^{12}\text{C}^{16}\text{O}$, the first five overtones of $^{12}\text{C}^{18}\text{O}$ (listed in Table 3.1), and C_2 absorption lines from the Phillips and Ballik-Ramsay systems. There is considerable blending of lines especially beyond 2.29 μm . Figure 1 shows a region with prominent CN lines for both dLHdC and RCB stars, along with a CN synthetic spectrum generated for one star in each class. Figure 2 shows a region dominated by $^{12}\text{C}^{16}\text{O}$ and $^{12}\text{C}^{18}\text{O}$ lines for the dLHdC and RCB stars. We also have several atomic lines in our spectra, however most of them are severely blended with molecular features. A few prominent ones that may be useful for recovering elemental abundances are listed in Table 3.1.

3.2. Spectral modeling

We constructed model synthetic spectra using a grid of hydrogen-deficient, spherically symmetric MARCS (Model Atmospheres in Radiative and Convective Scheme) atmospheric models, generated with input abundances of $\log \epsilon(\text{H}) = 7.5$, $\log \epsilon(\text{He}) = 11.5$, $\log \epsilon(\text{C}) = 9.5$ ($\text{C}/\text{He} = 0.01$), and $\log \epsilon(\text{O}) = 8.8$ (Gustafsson et al. 1975, 2008; Bell et al. 1976; Plez 2008).

¹ <https://dreams.anu.edu.au/monitoring/>

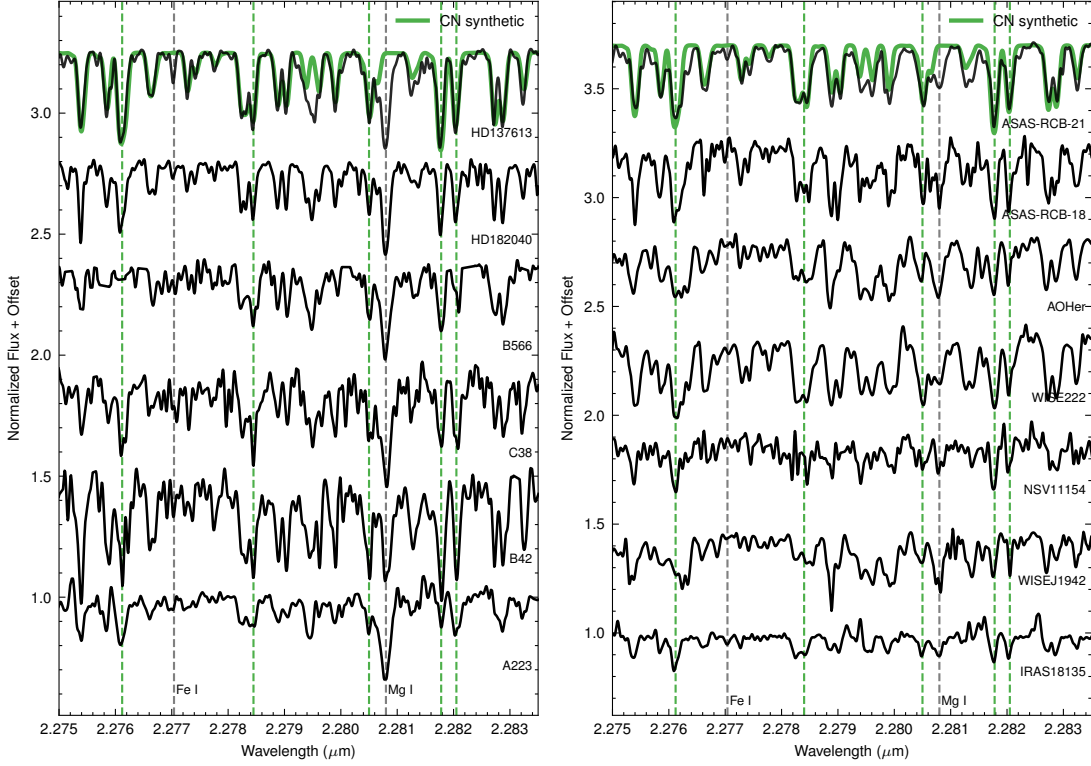


Figure 1. Spectra centred at $\sim 2.28 \mu\text{m}$ showing a region with $^{12}\text{C}^{14}\text{N}$ lines for the dLHdC stars (left) and RCB stars (right). $^{12}\text{C}^{14}\text{N}$ synthetic spectra generated for HD 137613 and ASAS-RCB-21 are overplotted in green for comparison, with a few strong lines marked. Also marked in gray are the locations of a few atomic lines.

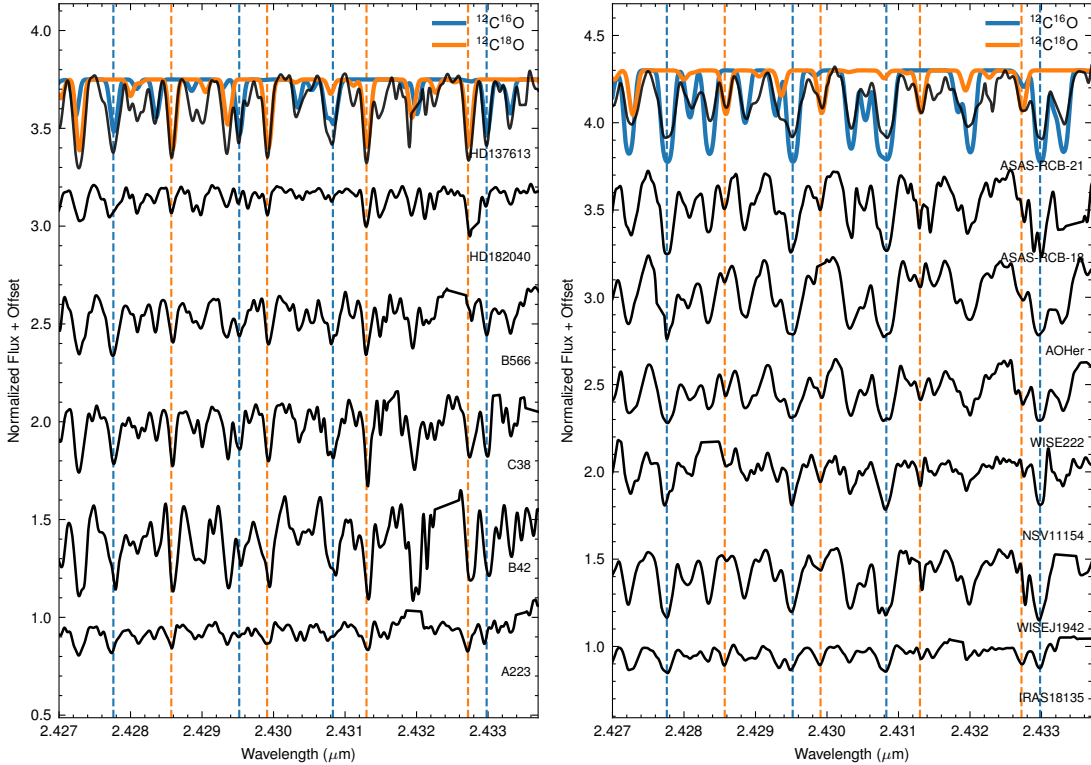


Figure 2. Spectra centred at $\sim 2.43 \mu\text{m}$ showing a region dominated by $^{12}\text{C}^{16}\text{O}$ and $^{12}\text{C}^{18}\text{O}$ lines for the dLHdC stars (left) and RCB stars (right). Individual synthetic spectra generated for HD 137613 and ASAS-RCB-21 are overplotted in blue and orange for comparison, with a few strong lines marked. It is clear that $^{12}\text{C}^{18}\text{O}$ is the dominant isotopologue in all dLHdC stars, while $^{12}\text{C}^{16}\text{O}$ is much more prominent in RCB stars. The line flattening effect visible at strong $^{12}\text{C}^{16}\text{O}$ lines for ASAS-RCB-21 is likely due to coincident emission lines from circumstellar gas, discussed in Section 4.2.

Table 1. Log of spectroscopic observations.

Name	Class	Date (UT)	S/N	Telluric Standard	Exposure Time (min)
HD 137613	dLHdC	2022-09-14	104	HIP79881	5.0
A223*	dLHdC	2022-09-14	127	HIP93667	57.5
B42*	dLHdC	2022-09-14	32	HIP93667	20.0
HD 182040	dLHdC	2022-09-22	108	HIP95793	3.0
C38*	dLHdC	2022-09-23	73	HIP93667	100.0
B566*	dLHdC	2022-09-30	78	HIP91137	90.0
WISE J1820+	RCB	2022-09-24	41	HIP93667	24.0
WISE J1942+	RCB	2022-09-22	98	HIP98953	50.0
IRAS 1813+	RCB	2022-09-22	149	HIP95793	50.0
ASAS-RCB-18	RCB	2022-09-23	79	HIP95793	13.5
V CrA	RCB	2022-09-23	136	HIP93470	10.0
AO Her	RCB	2022-09-24	88	HIP91315	10.0
ASAS-RCB-21	RCB	2022-09-24	81	HIP95793	27.0
NSV 11154	RCB	2022-09-24	87	HIP91315	54.0
WISE J1818+	RCB	2022-09-30	68	HIP93667	7.5

Note: The recently discovered dLHdC stars (Tisserand et al. 2022) are marked by asterisks. The following abbreviations are used throughout the text: WISE J194218.38-203247.5: WISE J1942+; IRAS 1813.5-2419: IRAS 1813+; WISE J181836.38-181732.8: WISE J1818+; WISE J182010.96-193453.4: WISE J1820+.

Table 2. Adopted stellar parameters.

Name	T_{eff} (K) ^a	$\log g$ (cm s ⁻¹)	ξ (km s ⁻¹)	v_{mac} (km s ⁻¹)
HD 137613	5500 ^b	1.0	6.5	0.0
HD 182040	5750	1.0	6.0	0.0
A223	6250	1.0	7.0	0.0
B566	5750	1.0	6.0	0.0
B42	5500	1.0	6.0	0.0
C38	5750	1.0	6.0	0.0
AO Her	4750 ^b	1.0	7.0	8.0
ASAS-RCB-18	5000	1.0	7.0	6.0
ASAS-RCB-21	5000	1.0	7.0	8.0
NSV 11154	5250	1.0	6.0	8.0
WISE J1818+	5000	1.0	7.0	5.0
WISE J1942+	4500 ^b	1.0	7.0	6.0

^a Chosen values are the nearest available from our grid of models. Values without a source in literature are adopted using empirical color-temperature calibration (Crawford et al. 2023)

^b References: Asplund et al. (1997), Bergeat et al. (2001), Karambelkar et al. (2021)

Species	Wavelengths (μm)
S I	2.2655, 2.2707, 2.2875
Si I	2.2665, 2.275, 2.3142, 2.3953, 2.4245, 2.4575
Fe I	2.262, 2.277, 2.2835, 2.331, 2.4164, 2.4265
Na I	2.3348, 2.338
Mg I	2.2808, 2.2906
C I	2.2642, 2.2685, 2.3436, 2.3443, 2.3613, 2.3736
$^{12}\text{C}^{16}\text{O}$	2.293, 2.322, 2.352, 2.382, 2.414, 2.445, 2.478
$^{12}\text{C}^{18}\text{O}$	2.349, 2.378, 2.408, 2.438, 2.469

Table 3. Locations of prominent features in our spectra.

The models were constructed for five different nitrogen abundance values of $\log \epsilon(\text{N}) = 7.0, 7.5, 8.0, 8.5,$ and 9.4^2 . A solar metallicity is assumed for other elements. The models assume a stellar mass of $1 M_{\odot}$, surface gravity values ($\log g$) = 1.0, microturbulence (ξ) = 5 km s^{-1} , and were computed for a grid of effective temperatures (T_{eff}) ranging from 4000 – 7500 K (in steps of 250 K).

We generated synthetic spectra using **TSFitpy** (Storm & Bergemann 2023) – a **python** wrapper around the radiative transfer package **Turbospectrum v20.0** (Alvarez & Plez 1998; Plez 2012; Gerber et al. 2023). We used the CO line list provided by B. Plez (priv. commun. and described in Goorvitch (1994)) and the ExoMol linelists for CN and C_2 (Yurchenko et al. 2018; Tennyson et al. 2024). Atomic line lists are generated using the VALD database (Ryabchikova et al. 2015).

3.3. Spectral Fitting

We fit the models to our observed spectra to derive the abundances of different elements. In addition to the elemental abundances, the model fitting requires four additional stellar parameters – effective temperature (T_{eff}), surface gravity ($\log g$), microturbulence (ξ), and macroturbulence (v_{mac}). The micro- and macroturbulence velocities are free parameters in our fitting and are estimated using the observed spectra (see below for details). We fix $\log g = 1.0$ for all stars, and use estimates of T_{eff} from literature where available. Table 2 lists the stellar parameters adopted for the stars analyzed here.

We convolve the synthetic spectra with a Gaussian function to match the iShell spectral resolution and fit the convolved models to our observed spectra using χ^2 minimization implemented in **TSFitpy**. We made some modifications to the default version of **TSFitpy** to include the synthetic spectra generated from our custom, sparse model grid. Specifically, we suppressed the inter-

polation of metallicity, $\log g$, and T_{eff} . We also modified the code to use $^{16}\text{O}/^{18}\text{O}$ ratio as a free parameter for fitting.

The carbon, nitrogen, oxygen abundances and oxygen isotope ratios for each star in our sample are derived using the following steps (illustrated in Figure 3 for HD 137613) –

1. An initial guess for the different elemental abundances is obtained by visually comparing the models with the observed lines.
2. The microturbulence (ξ) is determined using the method outlined in Kipper et al. (1996) (is Magain1984 the appropriate citation here?). A line-mask of single, unblended CN lines (or CO lines if a star has low $A(\text{N})$) is constructed. Models are fit to these lines to measure N (or O) abundances assuming different values of ξ . The value of ξ for which the slope between the derived abundances and the line equivalent widths is closest to zero is adopted as the microturbulence value for the star (see Figure 3(a)).
3. Clusters of partially blended neighboring lines are used to determine v_{mac} , as the profiles of such regions show the most prominent effects of any additional broadening. We find that dL-HdC stars do not show any broadening beyond instrumental resolution, while RCB stars indicate $v_{\text{mac}} \sim 5 - 8 \text{ km s}^{-1}$.
4. Next, $A(\text{C})$ is fit using a handful of weak, and CN-blended C_2 lines that appear to match our observed spectra. We find that the input $A(\text{C})$ value of 9.5 is too high for the cooler stars in our sample, and it was necessary to tweak this value on a star-by-star basis to obtain a good fit. These fits are done by keeping both C and N abundances as free parameters, as both elements affect the strengths of CN lines. See Figure 3(b) for an illustration. *This point needs to be modified, along with Fig 3b*
5. The obtained $A(\text{C})$ value is then used to fit a set of 30 – 40 CN lines to refine the nitrogen abundance. This is then fed back to the C_2 linemask fit to further improve the C abundance. This process is iterated a few times until the derived values converge. The uncertainty on the C and N abundances is obtained by measuring the standard deviation of the line-to-line scatter in the measured abundances.
6. Finally, the oxygen abundance and isotope ratio are fit using a linemask containing both $^{12}\text{C}^{16}\text{O}$

² Note: $\log \epsilon(\text{X})$ will be denoted by $A(\text{X})$

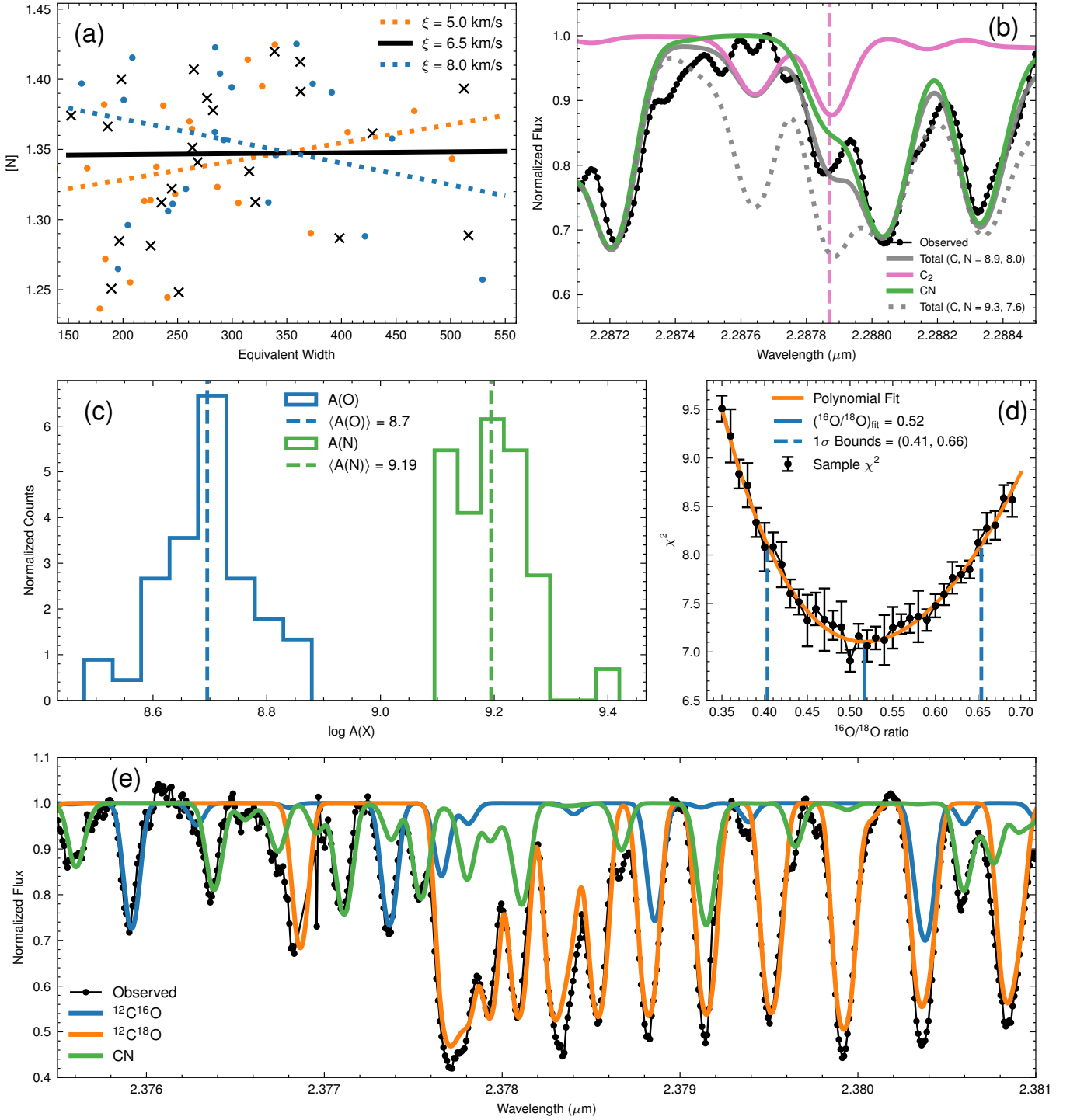


Figure 3. These panels show the steps discussed in Section 3.3 for HD 137613, except (b) which shows the cooler star, WISE J1818+ to better illustrate the $A(C)$ discrepancy.

(a) Equivalent Width v/s [N] obtained for 3 different ξ values, color-coded as per the legend with linear fits made to visually illustrate that the quantities are uncorrelated at the best-fit $\xi = 6.5$ km/s.

(b) The solid synthetic spectra (green is CN, pink is C_2 , gray is total) are computed using abundances chosen to fit the CN lines and the C_2 line marked in pink, while the dotted spectrum shows another best-fit spectrum obtained after increasing $A(C)$ by 0.4 dex – this change requires a reduction of $A(N)$ to maintain the fit, illustrating a degeneracy between the two.

(c) Distributions of fits obtained for $A(\text{O})$ and $A(\text{N})$ from the respective linemasks, with mean values marked.

(d) χ^2 curve obtained by fitting a range of $^{16}\text{O}/^{18}\text{O}$ ratios, with the best-fit value and 1σ bounds marked. The χ^2 values have errorbars as the final fits have an inherent spread caused by random sampling of initial guesses.

(e) Synthetic spectra generated for individual molecules compared with the observed data, indicating they are in agreement.

and $^{12}\text{C}^{18}\text{O}$ lines. Initially, the `a11` method is used to fit $A(\text{O})$ to the entire linemask for a grid of input $^{16}\text{O}/^{18}\text{O}$ ratios. A 4th order polynomial is fit to the resulting χ^2 vs $^{16}\text{O}/^{18}\text{O}$ curve to determine the best fit having the minimum χ^2 value, along with 1σ bounds using the $\Delta\chi^2 = 1$ criterion. The obtained isotope ratio is then used to fit $A(\text{O})$ to individual lines using the `1b1` method. Figure 3(c, d) illustrate the results from this process, and Figure 3(e) shows the final fits for individual molecules.

This process yields the abundances of nitrogen, oxygen, and the oxygen isotope ratio for each star in our sample, along with 1σ uncertainties for each quantity. Additionally, the atomic lines listed in Table 3.1 are used to obtain the abundances of Fe, Mg, Na, Ca, S, and Si. However, we are unable to measure accurate uncertainties for these elements because of the small number of their unblended absorption lines in our spectra. Based on the uncertainties for the CNO elements, we conservatively estimate an uncertainty of $\approx 0.3?$ dex on the abundances of these elements.

The measured elemental abundances and oxygen isotope ratios for the stars in our sample are listed in Table 4. We obtain consistent measurements for the two stars HD 137613 and HD 182040 that were analyzed previously using high-resolution spectra by García-Hernández et al. (2009). The CNO abundances and oxygen isotope ratios are precisely constrained for all stars in our sample, except WISEJ 1942+. For this star, the $^{12}\text{C}^{18}\text{O}$ lines are very weak compared to the $^{12}\text{C}^{16}\text{O}$ lines. This causes the χ^2 vs $^{16}\text{O}/^{18}\text{O}$ curve to flatten for large oxygen isotope ratios and never rises above the $\Delta\chi^2 = 1$ level from its minimum point. As a result, while we can measure the best-fit and $1-\sigma$ lower bound, the upper-bound on the $^{16}\text{O}/^{18}\text{O}$ is not constrained, and we report an upper limit of 500 for this star.

3.4. Sources of systematic errors

We now discuss the limitations of our analysis that are likely to introduce some systematic effects in the derived elemental abundances. We note that as these limitations have similar effects on the analyses of $^{12}\text{C}^{16}\text{O}$ and $^{12}\text{C}^{18}\text{O}$ lines, they should not significantly alter the oxygen isotope ratios, that are the main focus of our work.

3.4.1. Model Grid

The sparse grid of H-deficient stellar models available in the literature is a significant limitation in any elemental abundance study of HdC stars. It is clear that the range of input elemental abundances available in the

model-grid are not suitable for fitting the spectra of all HdC stars in our sample. For several stars, the derived abundances differ substantially from the input values assumed in the MARCS models. We cannot quantify the inaccuracies introduced by these deviations. A new set of HdC atmospheric models that span a wider range of elemental abundances is required to address this issue. The abundances derived in this paper will inform the choices for the new models.

The MARCS models used in our analysis were made with a fixed $A(\text{C})$ value of 9.5 that appears to be too high for the cooler stars in our sample. For example, we find $A(\text{C}) = 8.72$ for the RCB star WISEJ 1942+ with $T_{\text{eff}} = 4500$ K. Similar results were obtained by Pandey et al. (2021) in their analysis of the optical spectra of RCB stars, which also yielded several values lower than 9.5. Similarly, the fixed $A(\text{O})$ value of 8.8 chosen to generate the MARCS model appears to be too high for most of the stars in our sample. The majority of stars show $A(\text{O}) \sim 8.0$, with the lowest value obtained for the dLHdC star A223 at $A(\text{O}) = 7.0$. The few unblended atomic lines available in our spectra also seem to hint at variations in metallicity, with most RCB stars indicating $[\text{Fe}]$ ranging from -0.5 to -1.0 , while the dLHdC stars seem consistent with solar metallicity. This is another parameter that should be included in our model grid.

3.4.2. Stellar Parameters

To do: Add a table showing effects of varying T_{eff} , $\log g$, v_{mic} , v_{mac} on $A(\text{N})$, $A(\text{O})$, and O isotope ratio.

3.4.3. Carbon Problem?

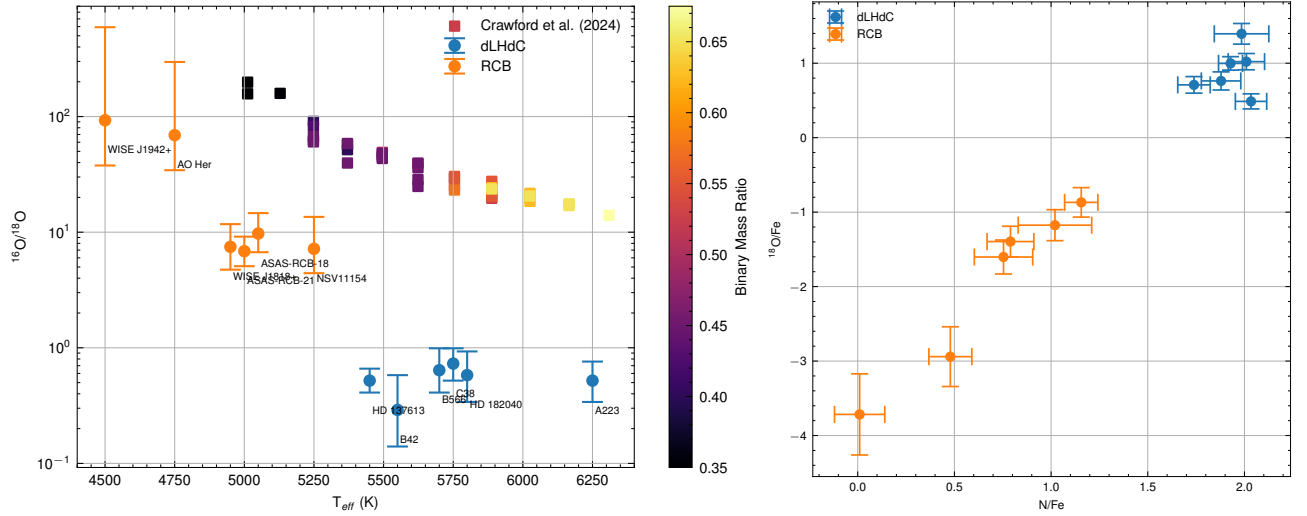
4. DISCUSSION

4.1. Oxygen Isotope ratios

The main goal of this paper was to measure precise oxygen isotope ratios for a large sample of RCB and dLHdC stars. Using our high-resolution spectra, we find that all dLHdC stars in our sample have oxygen isotope ratios lower by an order of magnitude than all RCB stars in our sample. All dLHdC stars in our sample have $^{16}\text{O}/^{18}\text{O} < 1$, while all RCB stars have $^{16}\text{O}/^{18}\text{O} > 4$. The coolest star in our sample RCB WISE J1942+ has a ratio as high as 92. Our results robustly confirm that dLHdC stars tend to have lower $^{16}\text{O}/^{18}\text{O}$ ratios than RCB stars – a trend suggested by previous analyses of medium resolution spectra (Karambelkar et al. 2022) and small samples of high-resolution spectra (García-Hernández et al. 2010). As noted previously, this difference can be explained by requiring that dLHdCs and RCBs originate in white-dwarf binaries with distinct properties such as total masses or mass-ratios (see Karambelkar et al. 2022; Crawford et al. 2023; Tisserand et al. 2022 for details).

Table 4. Chemical abundances and oxygen isotope ratios for the stars in our sample.

Name	T_{eff}	A(C)	A(N)	A(O)	$^{16}\text{O}/^{18}\text{O}$	[Fe]	[Mg]	[Na]	[Ca]	[S]	[Si]
HD 137613	5500	9.86 ± 0.12	9.24 ± 0.06	8.72 ± 0.08	$0.52^{+0.14}_{-0.11}$	-0.19	0.43	0.32	-0.22	-0.19	-0.38
HD 182040	5750	9.90 ± 0.13	9.08 ± 0.08	7.99 ± 0.06	$0.58^{+0.35}_{-0.24}$	-0.45	0.17	-0.02	-0.4	-0.15	-0.21
B566	5750	10.03 ± 0.25	9.09 ± 0.10	8.55 ± 0.10	$0.78^{+0.32}_{-0.23}$	0.23	0.74	0.62	0.04	0.18	0.20
C38	5750	10.32 ± 0.16	9.47 ± 0.08	8.99 ± 0.10	$0.73^{+0.26}_{-0.21}$	-0.78	-0.12	-0.12	-0.78	-0.38	-0.65
A223	6250	9.48 ± 0.24	8.73 ± 0.09	8.20 ± 0.09	$0.60^{+0.24}_{-0.19}$	-0.29	0.02	0.02	-0.52	-0.10	0.33
B42	5500	10.17 ± 0.14	9.18 ± 0.14	8.81 ± 0.1	$0.32^{+0.28}_{-0.15}$	-0.31	0.34	0.29	0.06	-0.10	0.03
NSV11154	5250	8.90 ± 0.06	7.45 ± 0.15	7.19 ± 0.10	$7.18^{+6.38}_{-2.76}$	-0.92	-1.37	-1.18	-1.11	-0.61	-1.11
ASAS-RCB-21	5000	8.86 ± 0.06	7.74 ± 0.09	7.77 ± 0.16	$6.85^{+2.30}_{-1.77}$	-0.80	-1.20	-1.56	-1.54	-0.12	-0.83
ASAS-RCB-18	5000	9.15 ± 0.05	7.83 ± 0.19	8.01 ± 0.14	$9.73^{+4.89}_{-3.02}$	-1.03	-1.28	-1.52	-1.74	-0.33	-0.14
WISE J1818+	5000	8.93 ± 0.06	7.60 ± 0.12	7.55 ± 0.10	$7.47^{+4.27}_{-2.73}$	-0.92	-1.23	-1.75	-1.56	0.01	-0.57
AO Her	4750	8.95 ± 0.05	6.95 ± 0.11	7.76 ± 0.14	69^{+228}_{-35}	-0.69	-1.22	-1.01	-0.90	-0.89	-0.38
WISE J1942+	4500	8.72 ± 0.06	6.59 ± 0.13	7.42 ± 0.10	93^{+500}_{-55}	-0.69	-1.31	-1.27	-0.86	-0.16	-1.00

**Figure 4.** Variation of isotope ratio with T_{eff} (left) and relative abundances of ^{18}O with N with respect to Fe (right) for the dLHdC (blue) and RCB (orange) stars in our sample. In cases where multiple stars have the same T_{eff} , offsets of 50 K have been applied for readability.

Recently, Crawford et al. (2024) explicitly studied the effect of total WD mass and WD mass-ratio on the observable properties of HdC stars by modeling CO-He white-dwarf mergers with total masses (M_{tot}) ranging from 0.675–0.825 M_{sun} and mass-ratios (q) ranging from 0.35–0.675. They find that lower M_{tot} and higher q mergers explain the observed lower luminosities and hotter effective temperatures of dLHdC stars, while also producing lower values of oxygen isotope ratios.

Additionally, we find a clear correlation between the oxygen isotope ratios and the effective temperatures of HdC stars (Figure 4), with warmer stars having lower $^{16}\text{O}/^{18}\text{O}$ ratios than the cooler ones. The two coolest stars ($T_{\text{eff}} \sim 4500$ K) have oxygen-isotope ratios that are an order of magnitude larger than the warmer ($T_{\text{eff}} >$

5000 K) stars. This is the first observed trend of oxygen isotope ratios in RCB and dLHdC stars. This trend of oxygen isotope ratios with the effective temperatures of HdC stars has also been predicted by the recent Crawford et al. (2024) theoretical models. They find that the lower q , higher M_{tot} mergers generally produce colder stars with higher oxygen isotope ratios, while high q , low M_{tot} mergers produce hotter stars with low oxygen isotope ratios. Fig. 4 also shows the oxygen isotope ratios as a function of effective temperatures from the Crawford et al. (2024) model grid. It is very promising that the models predict the same trend as the observations. However, as noted in Crawford et al. (2024), the exact values of the oxygen isotope ratios are not reproduced by the models. We note that the models overpredict

the observed oxygen isotope ratios by a factor of ≈ 2.5 . Crawford et al. (2024) suggest that the model oxygen isotope ratios can be reduced by adopting slightly lower helium-shell burning temperatures (T_{sof}).

4.2. Emission Line Contamination

In the spectra of RCB stars, we observe that the bottoms of strong $^{12}\text{C}^{16}\text{O}$ lines appear to be flattened or distorted at redder wavelengths, with the line cores appearing to be truncated while the wings still match synthetic spectra well. This effect is most prominent in ASAS-RCB-21, but visible to some extent in every RCB star within our sample. In general, the threshold flux level for this truncation rises as the wavelength increases, meaning more significant parts of the line are cut off, and more lines are affected at redder wavelengths, while weaker lines remain intact. Lines of similar strength at shorter wavelengths are not affected. *Todo: Add another figure to demonstrate this.*

Additionally, the effect is much more prominent at bandheads, which show large disagreements with synthetic spectra, even when lines of similar strength before the bandheads are well matched. No such behaviour is observed in dLHdC stars. Figure 5 compares prominent bandheads at similar wavelengths for ASAS-RCB-21 and HD 137613, highlighting the distortions observed in RCB stars. A pair of strong lines to the left of the bandhead are undistorted for ASAS-RCB-21, but the region after the start of the bandhead is significantly weaker than predicted, with a gradual improvement as we move away from it. In contrast, HD 137613 shows a near-perfect match for the entire wavelength range, even though the bandhead is significantly stronger. This rules out the possibility that the observed phenomenon is a saturation effect.

On careful examination of this phenomenon, we conclude that the truncation is most likely due to CO emission lines coming from a region located outside RCB stars' photosphere, either due to the hot corona or by the gas dragged away from the star during dust ejection episodes. These lines seem to be strong enough to flatten the cores of photospheric absorption lines. Similar narrow emission lines have been observed during maximal light and at the onset of declines in optical spectra of RCB stars by Kameswara Rao et al. (1999), along with broader emissions during minimum light (Kameswara Rao et al. 2004, 2006).

A similar effect was also observed in the spectrum of the RCB star ES Aql by García-Hernández et al. (2010), who attributed this to dilution due to the continuum emission from circumstellar dust, as this was accompanied by a K -band infrared excess. However, a simple

dilution or veiling effect does not fully explain the observed phenomenon, as we see that neighbouring lines of similar strength are impacted very differently, and the profiles of the lines are altered in ways that indicate contamination by emission lines as discussed earlier. Dilution would have a more uniform weakening effect across all lines, with a slight wavelength dependence only due to the shape of the dust blackbody spectrum. An example of this can be seen in the spectrum of IRAS 1813+ shown in Figures 1 and 2. If the strength of the emission lines scale with the circumstellar dust flux continuum, one would expect the effect to be stronger for RCB stars with larger infrared excess. This is indeed the case for ASAS-RCB-21, which has one of the highest infrared excesses in our sample, and is the star most affected by this phenomenon.

5. CONCLUSION

We analyzed NIR high-resolution spectra of six RCB and six dLHdC stars to determine their chemical abundances and oxygen isotope ratios. Using a grid of MARCS models for HdC stars, we fitted the observed spectra to obtain abundances of C, N, O, Fe, S, Si, Mg, Na, and Ca, along with the $^{16}\text{O}/^{18}\text{O}$ ratios using the radiative transfer code *Turbospectrum* and a modified version of the fitting package *TSFity*. This let us obtain robust estimates for elemental abundances, along with the oxygen isotope ratios for each star in our sample. Our work established with high confidence that the dLHdC stars have $^{16}\text{O}/^{18}\text{O}$ ratios < 1 , while the RCB stars have ratios > 4 , with the coolest RCB stars showing ratios as high as 100. We observed trends in the data that are consistent with the current understanding that partial Helium burning is responsible for the production of ^{18}O in HdC stars.

The extremely low $^{16}\text{O}/^{18}\text{O}$ ratios observed for dLHdC stars are not consistent with the predictions made by current white dwarf merger models, and an extension of these models to lower metallicities and initial abundances should be explored to potentially help explain these differences. Our work also highlights the need for a new generation of MARCS models with a wider grid of input abundances to accurately model the spectra of HdC stars. An extension to other $A(\text{C})$, $A(\text{O})$, and $[\text{Fe}]$ values is necessary to successfully analyze this diverse group of stars. This is a work in progress. One limitation of our sample is that the RCB stars are all cooler than 5250 K, while the dLHdC stars are warmer than 5500 K. This could potentially introduce biases in our results, and future high resolution observations of a more diverse sample of stars are needed to further verify findings such as the trend of $^{16}\text{O}/^{18}\text{O}$ with T_{eff} for RCB

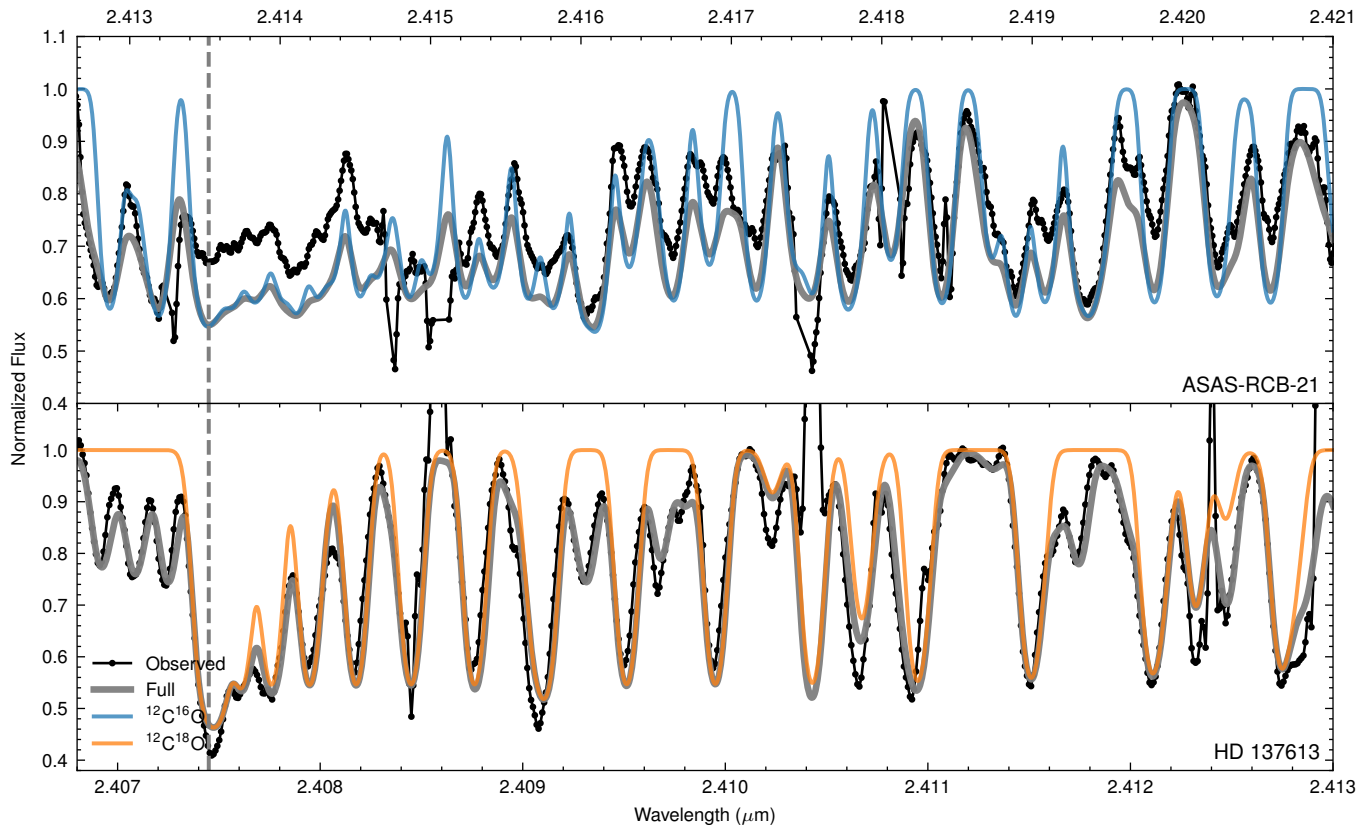


Figure 5. A comparison of strong bandhead of $^{12}\text{C}^{16}\text{O}$ (ASAS-RCB-21, top) and $^{12}\text{C}^{18}\text{O}$ (HD 137613, bottom) highlighting the distortions of deep lines observed in RCB stars. The location of the respective bandheads is indicated by a dashed vertical line.

stars. Moreover, the NIR band does not provide good coverage of atomic lines, and coordinated observations of the same stars in different bands could better constrain the abundances of several elements, which could together help solve some of the many puzzles posed by these enigmatic stars.

Also talk about ways to know more about the emission (spatially resolved spectra, similar study of how the lines evolve over time in R CrB, etc.)

6. APPENDIX

REFERENCES

- Alvarez, R., & Plez, B. 1998, *A&A*, 330, 1109
- Asplund, M., Gustafsson, B., Kiskelman, D., & Eriksson, K. 1997, *A&A*, 318, 521
- Bell, R. A., Eriksson, K., Gustafsson, B., & Nordlund, A. 1976, *A&AS*, 23, 37
- Bergeat, J., Knapik, A., & Rutily, B. 2001, *A&A*, 369, 178
- Clayton, G. C. 1996, *PASP*, 108, 225
- . 2012, *JAAVSO*, 40, 539
- Clayton, G. C., Geballe, T. R., Herwig, F., Fryer, C., & Asplund, M. 2007, *ApJ*, 662, 1220
- Clayton, G. C., Herwig, F., Geballe, T. R., et al. 2005, *ApJ*, 623, L141
- Crawford, C. L., Nikultsev, N., Clayton, G. C., et al. 2024, *arXiv e-prints*, arXiv:2408.09700
- Crawford, C. L., Tisserand, P., Clayton, G. C., et al. 2023, *MNRAS*, 521, 1674
- Cushing, M. C., Vacca, W. D., & Rayner, J. T. 2004, *PASP*, 116, 362
- García-Hernández, D. A., Hinkle, K. H., Lambert, D. L., & Eriksson, K. 2009, *ApJ*, 696, 1733
- García-Hernández, D. A., Lambert, D. L., Kameswara Rao, N., Hinkle, K. H., & Eriksson, K. 2010, *ApJ*, 714, 144
- Gerber, J. M., Magg, E., Plez, B., et al. 2023, *A&A*, 669, A43
- Goorvitch, D. 1994, *ApJS*, 95, 535
- Gustafsson, B., Bell, R. A., Eriksson, K., & Nordlund, A. 1975, *A&A*, 42, 407
- Gustafsson, B., Edvardsson, B., Eriksson, K., et al. 2008, *A&A*, 486, 951

- Kameswara Rao, N., Lambert, D. L., & Shetrone, M. D. 2006, *MNRAS*, 370, 941
- Kameswara Rao, N., Reddy, B. E., & Lambert, D. L. 2004, *MNRAS*, 355, 855
- Kameswara Rao, N., Lambert, D. L., Adams, M. T., et al. 1999, *MNRAS*, 310, 717
- Karambelkar, V., Kasliwal, M. M., Tisserand, P., et al. 2022, *A&A*, 667, A84
- Karambelkar, V. R., Kasliwal, M. M., Tisserand, P., et al. 2021, *ApJ*, 910, 132
- . 2024, *PASP*, 136, 084201
- Kipper, T., Jorgensen, U. G., Klochkova, V. G., & Panchuk, V. E. 1996, *A&A*, 306, 489
- Lambert, D. L., & Rao, N. K. 1994, *Journal of Astrophysics and Astronomy*, 15, 47
- Pandey, G., Hema, B. P., & Reddy, A. B. S. 2021, *ApJ*, 921, 52
- Plez, B. 2008, *Physica Scripta Volume T*, 133, 014003
- . 2012, *Turbospectrum: Code for spectral synthesis*, *Astrophysics Source Code Library*, record ascl:1205.004
- Rayner, J., Tokunaga, A., Jaffe, D., et al. 2022, *PASP*, 134, 015002
- Ryabchikova, T., Piskunov, N., Kurucz, R. L., et al. 2015, *Phys. Scr*, 90, 054005
- Schwab, J. 2019, *ApJ*, 885, 27
- Storm, N., & Bergemann, M. 2023, *MNRAS*, 525, 3718
- Tennyson, J., Yurchenko, S. N., Zhang, J., et al. 2024, *Journal of Quantitative Spectroscopy and Radiative Transfer*, 326, 109083
- Tisserand, P., Clayton, G. C., Bessell, M. S., et al. 2020, *A&A*, 635, A14
- Tisserand, P., Crawford, C. L., Clayton, G. C., et al. 2022, *A&A*, 667, A83
- Vacca, W. D., Cushing, M. C., & Rayner, J. T. 2003, *PASP*, 115, 389
- Yurchenko, S. N., Szabó, I., Pyatenko, E., & Tennyson, J. 2018, *MNRAS*, 480, 3397